Supplement of Atmos. Chem. Phys., 20, 7139–7152, 2020
https://doi.org/10.5194/acp-20-7139-2020-supplement

Atmospheric Chemistry and Physics
Open Access
EGU

Supplement of

Resonance-enhanced detection of metals in aerosols using single-particle mass spectrometry

Johannes Passig et al.

Correspondence to: Johannes Passig (johannes.passig@uni-rostock.de)

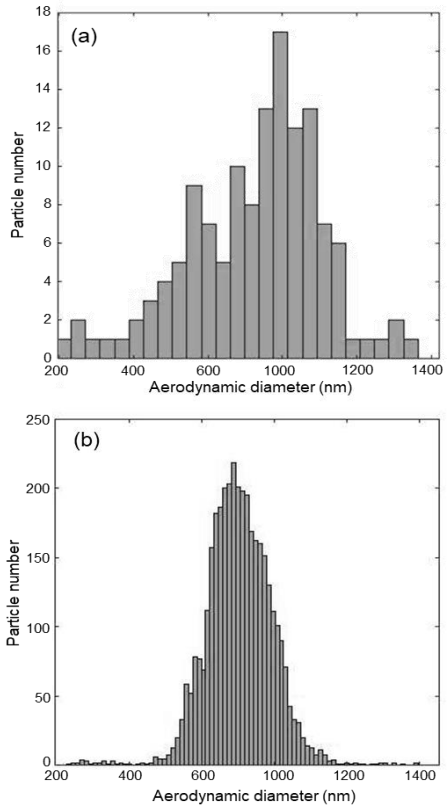

Figure S1: Particle size distributions for ambient air, measured with the optical detection unit of the SPMS at the site in Onsala, Sweden on the 09th Oct 2019 for each 1h, respectively; (a) without using the aerosol concentrator and (b) with the concentrator as described in the methods section. The real particle concentration factor in our experiment is obviously lower than the ratio of air intake and outlet volume (300:1).

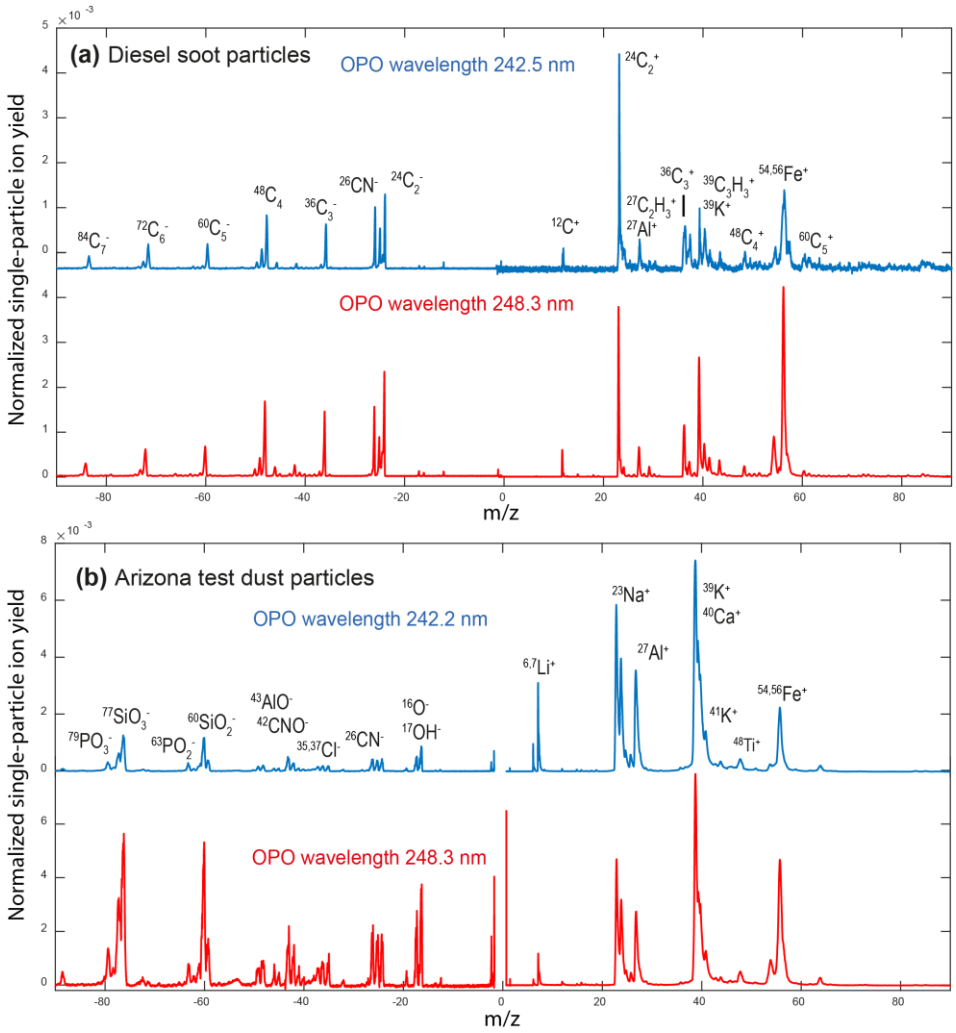

Figure S2: Averaged mass spectra (n=400) of the single-particle signal normalized to the total ion signal of each particle for (a) re-dispersed diesel soot (b) Arizona test dust particles.

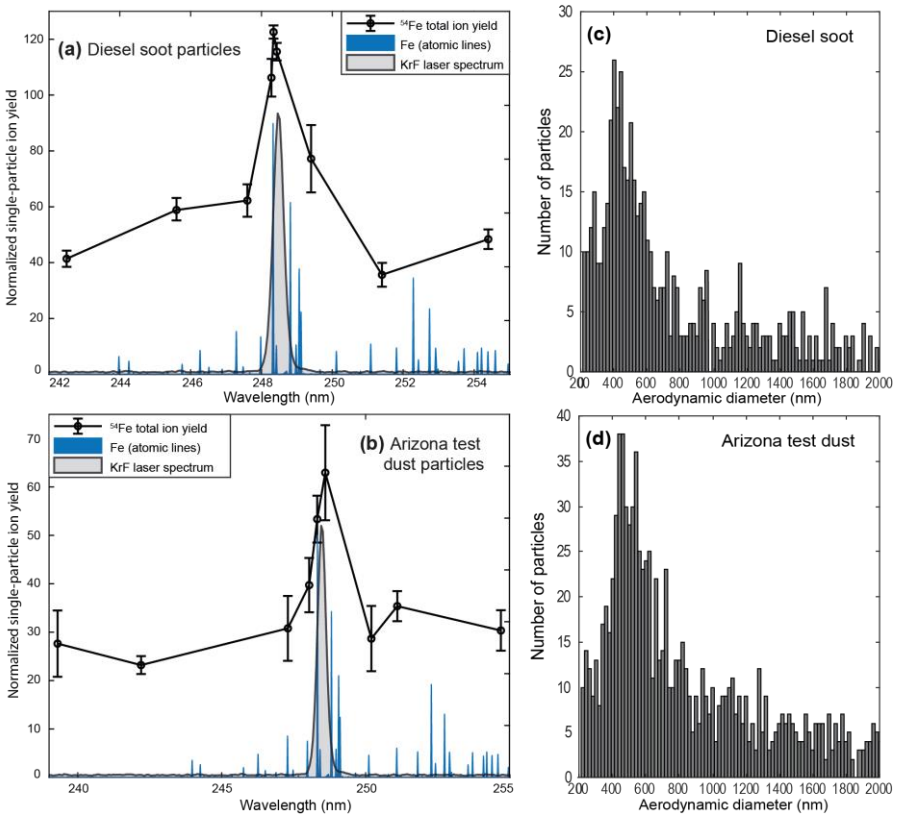

Figure S3: (a) Wavelength-dependent relative ion yield of ^{54}Fe (normalized to single-particle total ion signal) in SPMS of re-dispersed diesel soot particles (black circles, n=1200 in three replicates of 400 each). (b) The same results for Arizona desert dust particles. Major atomic transition lines of Fe in blue. Coincidentally, the Fe-lines are also addressed by our KrF-excimer laser (measured spectrum in grey, arbitrary units). Atomic spectra from the NIST library (Kramida and Ralchenko). Mass spectra are shown in Supplemental Figure S2.
(c) Size distribution of diesel soot particles, and (d) re-dispersed Arizona test dust particles, measured with the laser velocimetry sizing unit of the SPMS instrument.

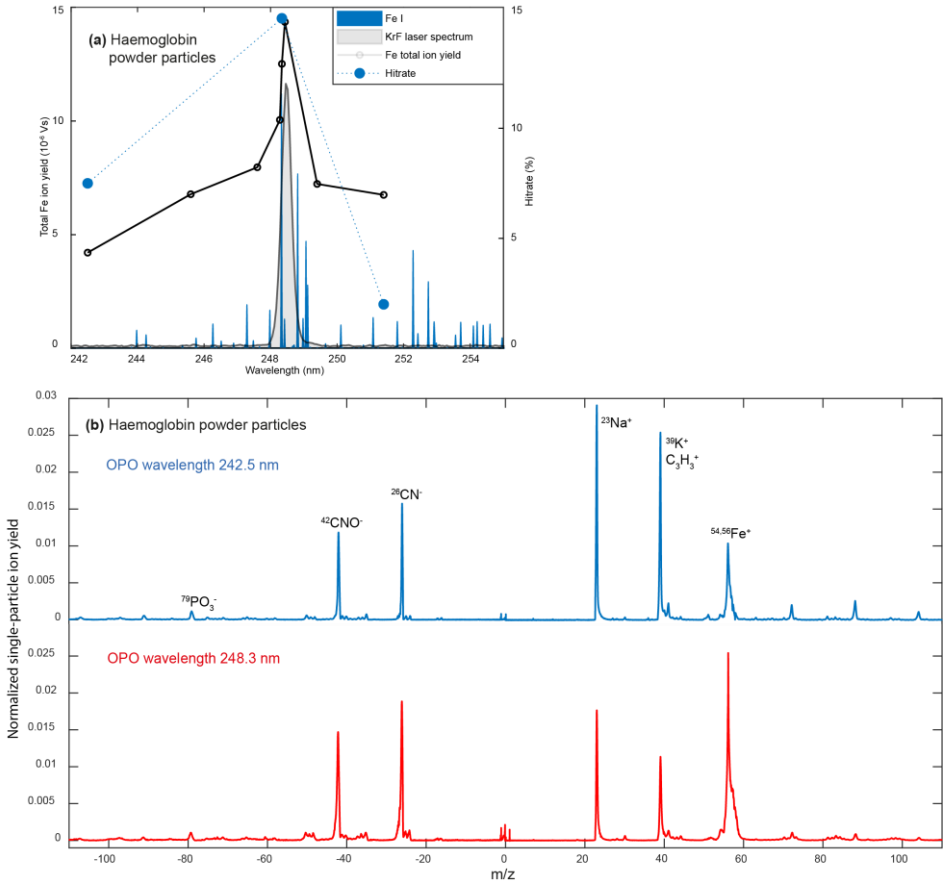

Figure S4: Results for hemoglobin from bovine blood (lyophilized powder, Merck Sigma Aldrich). (a) Wavelength-dependent total ion yield of ^{54}Fe (black circles, each n=250). The hit rate in this experiment (blue circles) dropped considerably for wavelengths above the Fe-resonance, complicating measurements beyond the resonance peak. However, the enhancement is clearly visible.
(b) Corresponding mass spectra for non-resonant (blue) and resonant (red) ionization, averaged over n=250 mass spectra, each normalized to single-particle total ion yield, respectively.

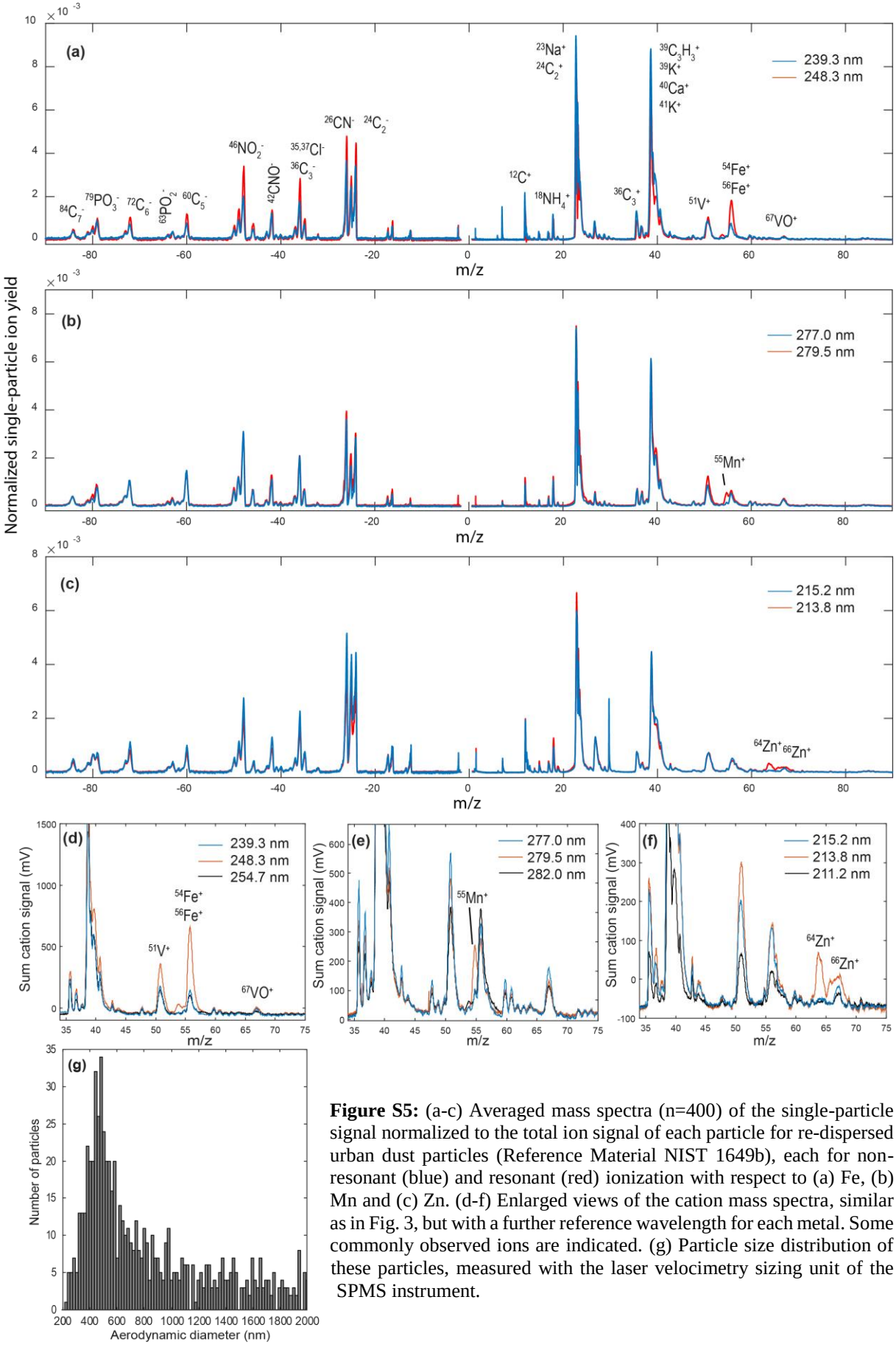

Figure S5: (a-c) Averaged mass spectra (n=400) of the single-particle signal normalized to the total ion signal of each particle for re-dispersed urban dust particles (Reference Material NIST 1649b), each for non-resonant (blue) and resonant (red) ionization with respect to (a) Fe, (b) Mn and (c) Zn. (d-f) Enlarged views of the cation mass spectra, similar as in Fig. 3, but with a further reference wavelength for each metal. Some commonly observed ions are indicated. (g) Particle size distribution of these particles, measured with the laser velocimetry sizing unit of the SPMS instrument.

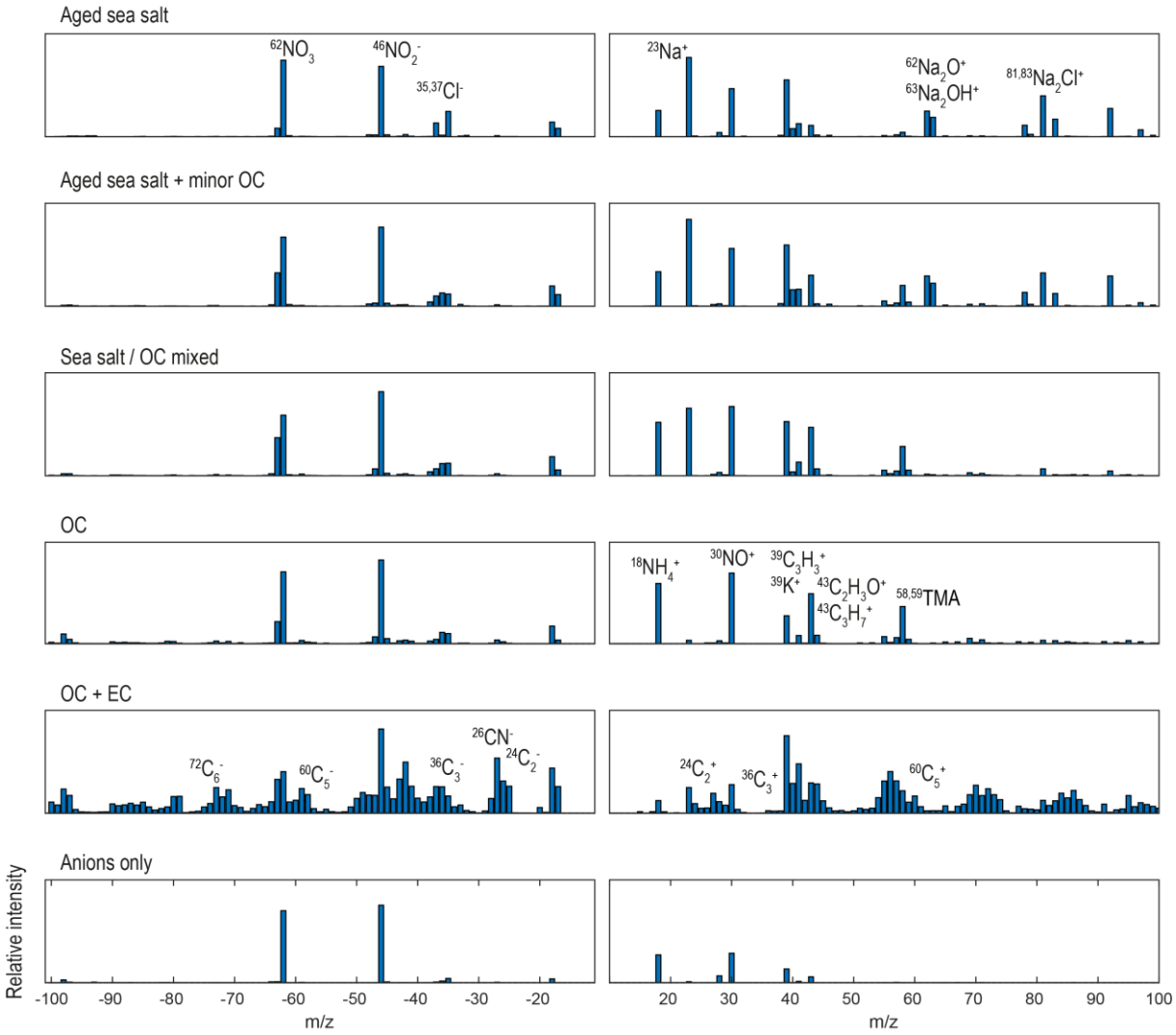

Figure S6: Main particle categories from the ambient air experiment with the 193 nm ArF laser after ART-2a clustering followed by manual merging with respect to the main compounds, see Table 2 for further details. Most particles were mixed of sea salt contributions, nitrate and organic fragments. EC signatures were detected in only 250 particles, along with strong fragment signals and partly with Fe signatures. They appeared occasionally over the full time and not within a single episode.

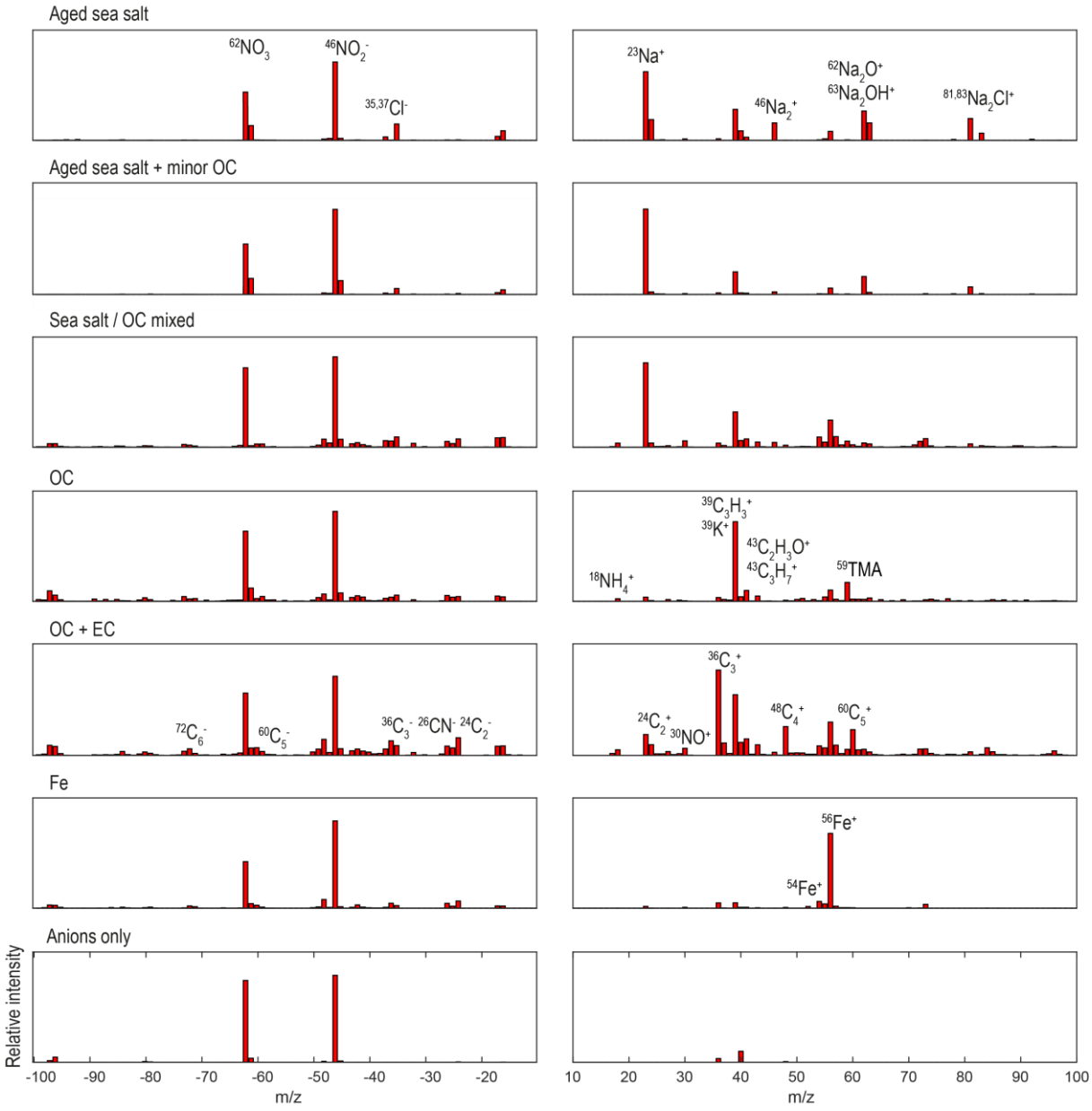

Figure S7: Main particle categories from the ambient air experiment with the 248 nm KrF laser after ART-2a clustering followed by manual merging with respect to the main compounds, see Table 2 for further details. Most particles were mixed of sea salt contributions, nitrate and organic fragments. Many particles that showed only anions (m/z=+54…56 were excluded from the ART-2a clustering) revealed exclusively Fe-signature in their cation spectra, contributing an own cluster. Fe-signatures appeared also for many particles with organic content. Differences between the two wavelengths beyond Fe-detection will be discussed in a future publication.

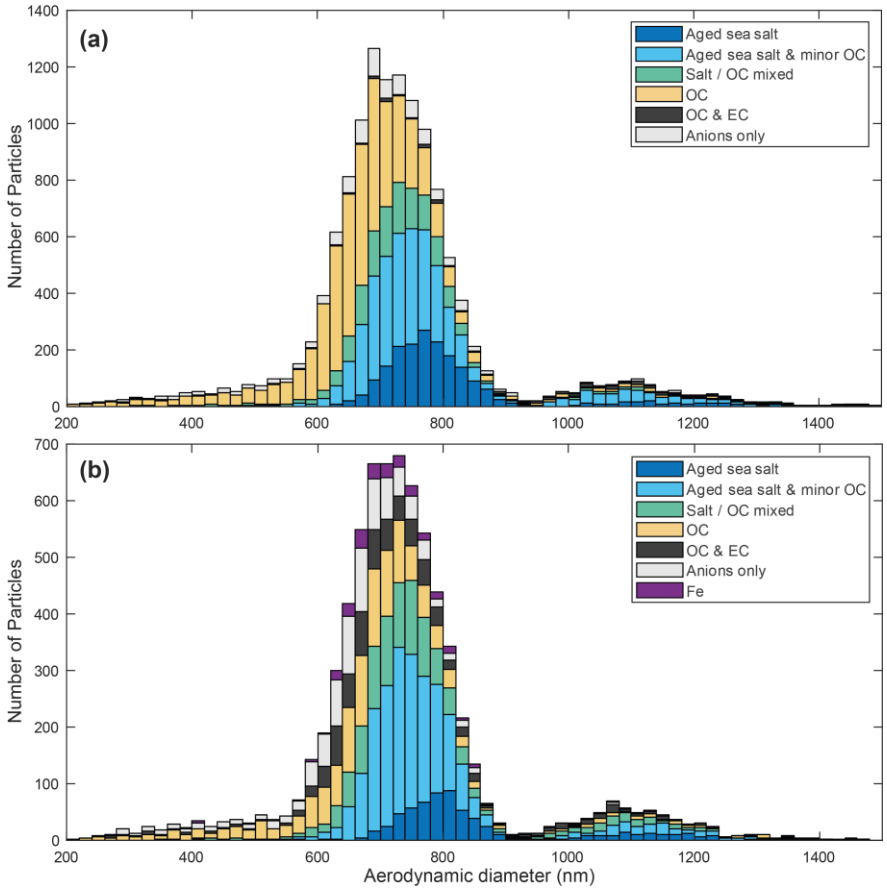

Figure S8: Particle size distribution of the main particle classes in the ambient air experiment; (a) for ionization with the 193 nm ArF-laser and (b) for the 248 nm KrF-laser. Note that the cutpoint for efficient aerosol concentration (≈0.5…1 µm), for optimum optical detection efficiency and the typical long-range transport size mode roughly coincide, thus the size distribution is rather narrow and biased by the instrument. However, it can be noticed that OC-dominated particles dominate the smaller size range while sea salt particles contribute mainly to the larger sizes and to the second mode at 1-1.2 µm.